

The topological Kondo model out of equilibrium

Matteo M. Wauters,^{1,2} Chia-Min Chung,^{3,4,5} Lorenzo Maffi,¹ and Michele Burrello¹

¹*Niels Bohr International Academy and Center for Quantum Devices, Niels Bohr Institute, Copenhagen University, Universitetsparken 5, 2100 Copenhagen, Denmark*

²*Pitaevskii BEC Center, Department of Physics, University of Trento, Via Sommarive 14, I-38123 Povo, Trento, Italy*

³*Department of Physics, National Sun Yat-sen University, Kaohsiung 80424, Taiwan*

⁴*Center for Theoretical and Computational Physics, National Sun Yat-Sen University, Kaohsiung 80424, Taiwan*

⁵*Physics Division, National Center for Theoretical Sciences, Taipei 10617, Taiwan*

The topological Kondo effect is a genuine manifestation of the nonlocality of Majorana modes. We investigate its out-of-equilibrium signatures in a model with a Cooper-pair box hosting four of these topological modes, each connected to a metallic lead. Through an advanced matrix-product-state approach tailored to study the dynamics of superconductors, we simulate the relaxation of the Majorana magnetization, which allows us to determine the related Kondo temperature, and we analyze the onset of electric transport after a quantum quench of a lead voltage. Our results apply to Majorana Cooper-pair boxes fabricated in double nanowire devices and provide nonperturbative evidence of the crossover from weak-coupling states to the strongly correlated topological Kondo regime. The latter dominates at the superconductor charge degeneracy points and displays the expected universal fractional zero-bias conductance.

The engineering of Majorana zero-energy modes (MZMs) in hybrid superconducting-semiconducting devices has been the core of strenuous theoretical and experimental activities for the last two decades [1–3]. The detection of these subgap modes relies primarily on tunneling spectroscopy applied to a rich variety of platforms, which, however, cannot provide direct evidence of the most intriguing properties of MZMs, namely their nonlocal and anyonic features. Hence, it is desirable to devise a new generation of experiments that balances the constraints imposed by the current technological limitations and the pursuit of MZM evidence beyond spectroscopy.

In this respect, the topological Kondo effect (TKE) [4–6] plays a crucial role: on one side, it is a transport signature of MZMs well-suited for experimental observations; on the other, it results from their nonlocality and can hardly be confused with phenomena originating by nontopological subgap states [7]. The TKE is predicted to emerge in multiterminal devices where M external leads are coupled to a Majorana Cooper-pair box hosting four MZMs and characterized by a charging energy E_c (Fig. 1). The TKE manifests itself as a universal nonlocal zero-bias conductance $dI_\alpha/dV_{\beta \neq \alpha}$ quantized at values $2e^2/Mh$. Such conductance is approached at low temperatures in correspondence of both the Coulomb valleys and peaks of the related devices [8], as derived from renormalization group (RG) analyses of effective low-energy models describing the Majorana Cooper-pair box coupled to M leads [4–6, 8–12].

In this letter, we address the experimental observability of the TKE from a more elementary and microscopic perspective and we examine its onset out of equilibrium. We characterize the quantum-quench dynamics of a minimal interacting fermionic model that includes both MZMs and quasiparticle excitations above the superconducting gap. The time evolution is determined

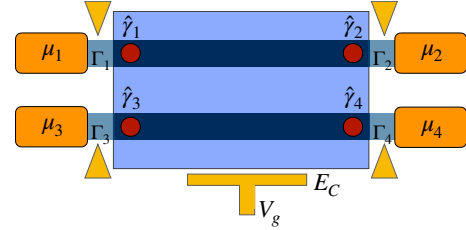


Figure 1. Schematics of the system: two p-wave superconducting nanowires with MZMs at the edges are coupled by a SC island (blue) with charging energy E_c . Voltage gates (yellow) tune the island induced charge, $n_g \propto V_g$, and the coupling rates Γ_α with the leads (orange). Each MZM is coupled with a single normal lead at chemical potential μ_α .

by electrons tunneling from the leads to the superconducting (SC) island, and, differently from previous TKE studies [4, 6, 10, 13–16], we apply matrix-product-state (MPS) simulations [17] which do not rely on any perturbative approximation of this coupling nor on a clear energy scale separation. This technique allows us to examine the crossover between the predicted weak-coupling and topological Kondo strong-coupling regimes and estimate the related topological Kondo temperature T_K .

The model we propose provides a minimal description of Majorana Cooper-pair boxes engineered from nanowires. Recent developments in the fabrication of parallel InAs nanowires hybridized with Al [18, 19] make these platforms suitable to combine all the necessary elements to implement of the topological Kondo model. It is therefore important to investigate its transport signatures as a function of the most relevant experimental parameters: lead voltages, charge induced on the SC island, and lead-island couplings.

a. Model and methods.- We consider a TKE model composed by two parallel 1D topological superconductors coupled by a common floating SC island with charging energy E_c and charge n_g induced by the potential V_g (Fig. 1). It describes two nanowires with strong spin-orbit coupling subject to a proximity-induced SC pairing and a suitable Zeeman interaction, which provide a common route to engineer MZMs [20, 21]. Their low-energy physics is captured by spinless fermions subject to an emergent p-wave SC pairing Δ_P . As a result, four MZMs $\{\gamma_\alpha\}_{\alpha=1,\dots,4}$ form at the nanowire edges, each coupled to a spinless normal lead. The tunneling rates Γ_α between leads and MZMs can be switched off to change the number of terminals $M \leq 4$ coupled to the system.

The simplest description for each SC nanowire is a zero-bandwidth model [22–24], where the lowest energy level is the subgap state defined by two Majorana operators, while the higher energy state represents Bogoliubov quasiparticles above the SC gap. This corresponds to a 2-site Kitaev chain for each nanowire, with each of the four constituting fermionic sites tunnel-coupled to one of the leads. This system defines the SC box sketched in Fig. 1, with Hamiltonian $\hat{H} = \hat{H}_{\text{sys}} + \hat{H}_L + \hat{H}_t$. \hat{H}_{sys} describes the Majorana Cooper-pair box [25, 26]:

$$\hat{H}_{\text{sys}} = \sum_{\sigma,n} \epsilon_{n,\sigma} \hat{f}_{n,\sigma}^\dagger \hat{f}_{n,\sigma} + E_c (\hat{N} - n_g)^2, \quad (1)$$

where $\sigma = \uparrow, \downarrow$ labels the upper and lower nanowires and $n = 0, 1$ the two quasiparticle states in each of them [27]. \hat{N} is the total box charge with respect to an arbitrary offset. It includes both its Cooper pairs and the electrons in the nanowires.

The two zero-energy quasiparticles are generated by the combinations of MZMs $\hat{f}_{0,\uparrow} = (\hat{\gamma}_1 - i\hat{\gamma}_2)/2$ and $\hat{f}_{0,\downarrow} = (\hat{\gamma}_3 - i\hat{\gamma}_4)/2$. We label the four corresponding low-energy states by $|n_\uparrow n_\downarrow\rangle$, with $\hat{n}_\sigma = \hat{f}_{0,\sigma}^\dagger \hat{f}_{0,\sigma}$. The charging energy splits them into two degenerate pairs with different fermionic parity $(-1)^{\hat{N}}$. Hereafter, we set equal SC pairing and nanowire hopping, $\Delta_P = t_{\text{sys}} = 0.5t_0$, and introduce a small potential $\mu_{\text{sys}} = 0.01t_0$ [27].

The leads are modeled by Wilson chains [17, 28, 29]

$$\hat{H}_L = \sum_{\alpha=1}^4 \sum_{l=1}^{\mathcal{L}} \left[-t_0 e^{-(l-1)/\xi} \hat{c}_{\alpha,l+1}^\dagger \hat{c}_{\alpha,l} + \text{h.c.} \right] - \mu_\alpha \hat{c}_{\alpha,l}^\dagger \hat{c}_{\alpha,l}, \quad (2)$$

with t_0 being the *bare* hopping amplitude which sets their bandwidth and constitutes the largest energy scale. The hopping decay length ξ is an auxiliary variable allowing us to tune the resolution at small energies by modifying the lead level spacing [17, 29, 30]. The chemical potentials μ_α are used to bring the system out of equilibrium and study transport properties.

The tunneling Hamiltonian between the leads and the

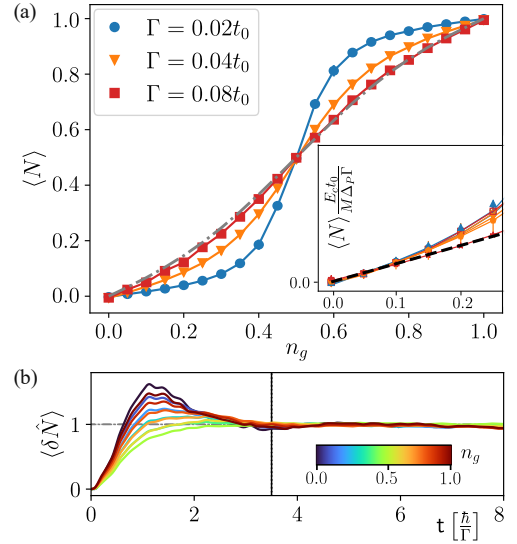


Figure 2. (a) Equilibrium charge versus n_g , for $M = 3$, $E_c = 0.2t_0$. The gray dot-dashed line corresponds to Eq. (4) for $\Gamma = 0.08t_0$. Inset: data for different values of E_c ($0.2t_0$ and $0.4t_0$) and $M = 3, 4$ in the weak-coupling regime, rescaled by $\frac{M \Delta_P \Gamma}{E_c t_0}$. The dashed black line corresponds to $\langle \hat{N} \rangle = \frac{M \Delta_P \Gamma}{E_c t_0} n_g$. (b) Charge relaxation for different values of $n_g \in [0, 1]$, $E_c = 0.2t_0$ and $\Gamma = 0.04t_0$. All data are obtained with $\mathcal{L} = 64$ and $\xi = 16$.

system is

$$\hat{H}_t = - \sum_{\alpha=1}^4 \sum_{\sigma,n} J_\alpha \left[\left(u_{\alpha,\sigma,n} \hat{f}_{\sigma,n}^\dagger + v_{\alpha,\sigma,n} \hat{f}_{\sigma,n} \right) \hat{c}_{\alpha,1} + \text{H.c.} \right], \quad (3)$$

where $u_{\alpha,\sigma,n}$ ($v_{\alpha,\sigma,n}$) is the particle (hole) projection of $\hat{f}_{\sigma,n}$ on the real-space site coupled to lead α . The amplitudes J_α determine the effective tunneling rates $\Gamma_\alpha = \frac{J_\alpha^2}{2t_0}$.

In our simulations, we map the system into an MPS by following Refs. [17, 30]. Each MPS site represents a single-particle eigenstate of either the leads or the nanowires (Bogoliubov quasiparticles for nanowires) and we order them based on their energy. The charge \hat{N} is encoded in an auxiliary site [27, 31]. The real-time dynamics is simulated using the time-dependent variational principle algorithm [32–34] from the ITensor library [35, 36]. We set the MPS truncation error $\sim 5 \cdot 10^{-8}$, corresponding to a maximum bond dimension $\chi \lesssim 2000$.

b. Relaxation towards equilibrium.- In the Kondo problem dynamics, the formation of strong correlations and the Kondo screening cloud occurs over a timescale given by T_K^{-1} [30, 37–39]. Therefore, the relaxation after a quantum quench offers a useful probe to estimate the Kondo temperature and detect strongly correlated states.

In the following, we consider the dynamics of the system in a post-quench non-equilibrium quasi-steady state

(NEQSS). In this regime, the time-evolution fulfills a Lieb-Robinson bound [40, 41] such that the dynamics is not affected by finite-size limitations until the signal propagates to the edge of the simulated system. Due to this, the information acquired from the analysis of the NEQSS well represents the out-of-equilibrium physics in the thermodynamic system (see, for instance, Refs. [42–45]), as verified also by applying our protocol to superconducting interacting scatterers [17] and the Anderson impurity model [30].

The first quench protocol we consider aims at observing the relaxation of the Majorana Cooper-pair box caused by \hat{H}_t . The box is initialized in the ground state $|00\rangle$ ($N = 0$ for $n_g < 0.5$) or $|10\rangle$ ($N = 1$ for $n_g > 0.5$) and is decoupled from the leads, which are set at half-filling. At time $t = 0$, the couplings Γ are suddenly turned on and the device begins relaxing toward equilibrium. To characterize this relaxation, we analyze the average island charge $\langle \hat{N}(t) \rangle$, and the effective Majorana magnetization [4, 13] $\langle \hat{Z}_{\text{eff}}(t) \rangle \equiv \langle i\hat{\gamma}_3\hat{\gamma}_4(t) \rangle = 1 - 2\langle \hat{n}_\downarrow(t) \rangle$.

The observed dependence of $\langle \hat{N} \rangle$ on n_g after equilibration (Fig. 2) shows the crossover between the weak-coupling and the strong-coupling regime. Following Ref. [46], we characterize the weak-coupling regime at $n_g \sim 0$ by the slope of $\langle \hat{N} \rangle = \frac{M\Delta_P\Gamma}{E_c t_0} n_g$: For weak Γ , the charge datasets corresponding to different choices of E_c and M [47] exhibit a good agreement with the expected linear dependence [inset of Fig. 2(a)]. On the other hand, the sinusoidal correction derived for the strong-coupling regime [46],

$$\langle \hat{N} \rangle = n_g - \left(\frac{E_c}{\Delta_P} \sqrt{1 - \Gamma/t_0} \right)^M \sin(2\pi n_g), \quad (4)$$

closely matches the numerical data for the highest value of the tunneling rate $\Gamma = 0.08t_0$ [gray dot-dashed line and red squares in Fig. 2(a)], thus suggesting the emergence of Kondo correlations.

Importantly, the relaxation timescale of $\langle \hat{N} \rangle$ depends on the ratio Γ/E_c but not on the induced charge n_g , as shown in Fig. 2(b) which displays the time dependence of the relative charge variation,

$$\langle \delta \hat{N}(t) \rangle = \frac{|\langle \hat{N}(t) \rangle - \langle \hat{N}(0) \rangle|}{|\langle \hat{N}(t \rightarrow \infty) \rangle - \langle \hat{N}(0) \rangle|}. \quad (5)$$

The vertical line marks the equilibration time and different curves, corresponding to different values of $n_g \in [0, 1]$, converge to $\langle \delta \hat{N}(t) \rangle = 1$ on similar timescales.

The magnetization, instead, displays a remarkably different behavior [Fig. 3(a)]. At short times, $t < \hbar/\Gamma$, the relaxation is dominated by the fast rate Γ (dot-dashed line) independently of both E_c and n_g . Then, a second timescale emerges, which depends on both Γ and the energy difference $\delta E(n_g) = E_c|1 - 2n_g|$ between the charge sectors $N = 0$ and $N = 1$. The black dashed lines in

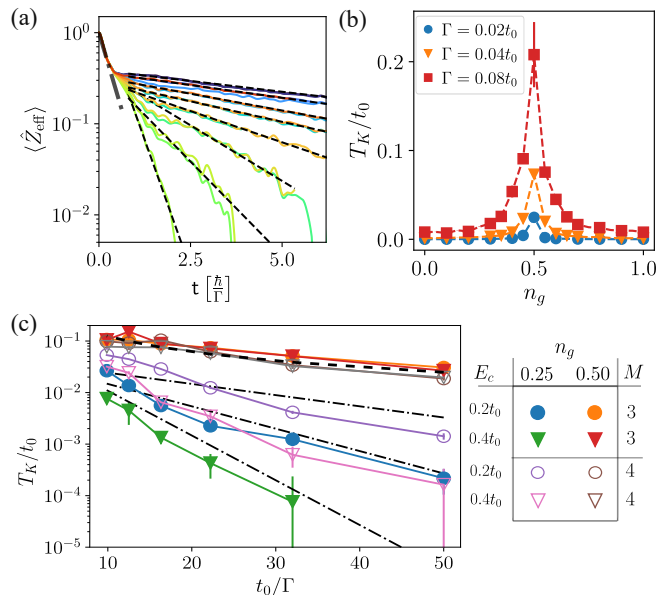


Figure 3. (a): Dynamics of the Majorana magnetization for different values of $n_g \in [0, 1]$; $E_c = 0.2t_0$ and $\Gamma = 0.08t_0$. The dot-dashed line marks the decay rate Γ . (b) T_K extracted as the relaxation rate of $\langle \hat{Z}_{\text{eff}} \rangle$ —dashed lines in panel (a)—as a function of n_g . (c) T_K as a function of t_0/Γ at $n_g = 0.5$ and in the even-parity Coulomb valley ($n_g = 0.25$). Dot-dashed lines correspond to Eq. (6), whereas the dashed line marks the degeneracy point scaling $T_K \sim M\Gamma$. A prefactor $C \sim 0.2$ has been manually set to approximately match the data. All data are obtained with $\mathcal{L} = 64$, $\xi = 16$.

Fig. 3(a) are exponential fits of these slower decays. This behavior is analogous to the magnetization relaxation in the Anderson impurity model [30, 38, 48], suggesting that this longer timescale is associated with the energy scale T_K of the emerging TKE.

The comparison of Figs. 3(a) and 2(b) underlines that this Kondo timescale characterizes only the Majorana magnetization but not the charge; $\langle \hat{Z}_{\text{eff}} \rangle$ constitutes indeed one of the effective Pauli operators at the heart of the definition of the TKE, whereas $\langle \hat{N} \rangle$ depends only on the fermionic parity of the SC island. Therefore, we interpret this charge - “spin” separation as evidence of the TKE emergence.

Next, we analyze the dependence of the so-derived T_K on n_g , Γ , and E_c . Figure 3(b) depicts the fitted T_K as a function of n_g for different values of Γ and $E_c = 0.2t_0$. As expected from RG analyses, T_K is larger at the charge degeneracy point where it is proportional to $M\Gamma$, consistently with Ref. [46]. In the Coulomb valleys, instead, T_K is qualitatively compatible with standard RG predictions [46]:

$$T_K \sim E_c e^{-\frac{\delta E(n_g)t_0}{2(M-2)\Gamma\Delta_P}}. \quad (6)$$

The different behaviors at the charge degeneracy point ($n_g = 0.5$) and in the even Coulomb valley ($n_g = 0.25$) are exemplified in Fig. 3(c), which displays T_K versus

t_0/Γ for two values of E_c and M (see legend). T_K extracted at $n_g = 0.5$ is independent of both E_c and M and it decreases with a power law compatible with $T_K \sim \Gamma$ (dashed line). For large values of Γ , the magnetization can change sign, preventing us from extracting T_K with high precision (see the large errorbar at $n_g = 0.5$ in Fig. 3(b)). In the Coulomb valleys, instead, T_K shows a substantial drop when increasing E_c : not only it is smaller for $E_c = 0.4t_0$, but it decreases faster with $1/\Gamma$, in accordance with Eq. (6) (dot-dashed lines). The data for $M = 4$, $E_c = 0.4t_0$ and $M = 3$, $E_c = 0.2t_0$ almost coincide as Eq. (6) predicts the same behavior but for a factor 2 in front. Our data display a concavity that is absent in Eq. (6) and suggests a competing power law dependence on Γ in agreement with NRG results of the low-energy effective model [10]. The presence of a power-law correction can also be understood as the interpolation between the scaling of T_K deep in the Coulomb valleys, where it is dominated by the exponential decay, and that at $n_g = 0.5$, where it is proportional to Γ . At intermediate values of the induced charge, $0 < n_g < 0.5$, we expect a gradual crossover between the two regimes when the coupling strength Γ becomes comparable with the charge excitations, as either Γ increases or the charge degeneracy point is approached.

c. Nonlocal transport.- To investigate multiterminal transport properties, we adopt a different quench protocol, using DMRG to prepare the ground state of the device coupled with M leads at equilibrium ($\mu_\alpha = 0$). In general, such a state is a superposition of different charge and magnetization states. At $t = 0$ we quench the chemical potential in the first lead to a finite value $\mu_1 = eV_b$ and compute the average current flowing through the remaining connected terminals. We refer to the latter as average nonlocal current.

RG predicts a fractional zero-bias nonlocal conductance, $G_{\text{TKE}} = \frac{2}{M} \frac{e^2}{h}$, independent from all other physical parameters for $T \ll T_K$, both in the Coulomb valleys [4–6], and at the charge-degeneracy points [8, 11, 16, 46]. Our simulations capture this fractional conductance for $M = 3, 4$ for sufficiently strong coupling in proximity of $n_g = 0.5$, where T_K is maximum and G_{TKE} can be observed for an extended voltage bias window (Fig. 4). For $n_g \sim 0.5$, we also observe non-Fermi liquid power-law corrections with noninteger exponents which, however, do not seem compatible with the first-order scaling predicted by bosonization and RG [8, 11, 15, 16, 27, 46, 49].

Our simulations are performed at zero temperature, but, away from $n_g = 0.5$, T_K becomes comparable with the energy we introduce with the finite bias eV_b , competing with the universal strong-coupling features of the model. In Fig. 5 we plot the average nonlocal current ($M = 3$ and $E_c = 0.4t_0$) divided by the voltage bias as a function of n_g . We set $\mu_1 = eV_b = 0.02t_0$, which is small enough to probe the response close to the linear regime, yet the data display a good signal-to-noise ratio. The TKE prediction is met at the charge degeneracy point and strong coupling, consistently with Fig. 4, while the

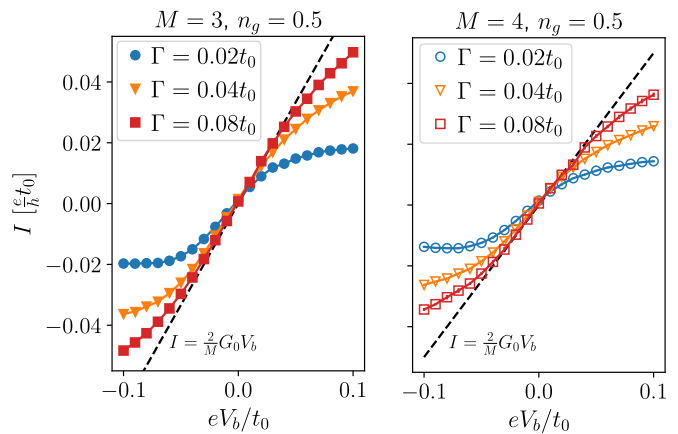


Figure 4. Average nonlocal current versus V_b at $n_g = 0.5$, for $M = 3, 4$. The dashed line highlights the TKE prediction $G = \frac{2}{M}G_0$. The data are obtained with $\mathcal{L} = 100$ and $\xi = 32$.

strong n_g dependence confirms that we are not deep in the TKE regime; however, several hints of a strongly-correlated Kondo state emerge also in the Coulomb valleys.

In Fig. 5, we compare our data with the conductance G_{RL} of a single fermionic resonant level (RL), which exhibits a peak scaling as $4G_0/M^2$ with width $\sim M\Gamma/E_c$ (dashed lines) [27]. The data with the weakest coupling ($\Gamma = 0.02t_0$) match well the RL approximation, as expected in a weak-coupling regime. By increasing Γ , we observe large deviations from the single RL and the conductance rapidly approaches the TKE value of $\frac{2}{3}G_0$ (horizontal dot-dashed line) for $n_g \sim 0.5$. Indeed, in this regime, the applied voltage $\mu_1 = 0.02t_0$ is one order of magnitude smaller than the estimate of the Kondo temperature, $T_K \sim 0.1t_0$ in Fig. 3(c). Moreover, there is a substantial current flowing deep in the Coulomb valleys ($\Gamma = 0.08t_0, 0.04t_0$) with apparent plateaus that suggest a crossover to the TKE regime. This is further confirmed by the analysis of the data averaged over the decay length ξ [27].

The main difficulty for our approach in investigating a deeper Kondo regime in the Coulomb valleys stems from the very low voltage bias needed to probe energy scales that are exponentially suppressed in $\delta E(n_g)$ as T_K . Indeed, finite-size effects limit the resolution in eV_b that we can achieve and hinder the observation of Kondo physics at small coupling or deep in the Coulomb valleys. Hence, our method is complementary to NRG: while the latter is more suited for studying the universal features of relevant low-energy approximations, our approach allows for a more direct comparison with experiments that have to cope with the interplay and possible competition between different energy scales.

In the supplemental materials [27], we show the robustness of the TKE features against coupling anisotropies and the TKE disappearance when the MZMs acquire an energy splitting.

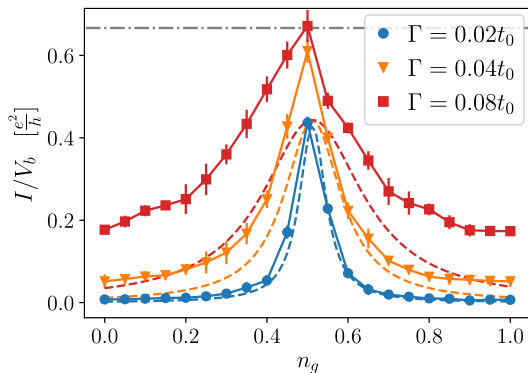


Figure 5. Nonlocal current versus n_g , for $E_c = 0.4t_0$. The dashed lines are the corresponding RL approximation [27]. The horizontal dot-dashed line is $\frac{2e^2}{hM}$ with $M = 3$.

d. Conclusions.- We analyzed the out-of-equilibrium properties of a minimal model for the topological Kondo effect, aiming at a microscopic description alternative to RG approaches and a qualitative understanding of transport signatures that may arise in double nanowire experiments. Our results present evidence of the onset of strongly-correlated states compatible with a crossover between a weak-coupling and a topological Kondo regime.

First, the charge and the effective magnetization of the Majorana Cooper-pair box are characterized by different relaxation behaviors: the former only depends on the system-leads hybridization Γ , whereas the latter presents two separate timescales. In analogy with the dynamical features of the Anderson impurity model, we used the longer timescale to estimate the Kondo temperature associated with the TKE, with results compatible with the RG predictions [4, 6].

Second, the nonlocal conductance in the intermediate to strong-coupling regimes matches the predicted value $G_{\text{TKE}} = 2G_0/M$ at the charge degeneracy point, where T_K is the largest. In the Coulomb valleys, it presents large deviations from the noninteracting resonant level approximation that well describes the weak-coupling regime and two-terminal devices [17]. When the resonant level approximation fails, the conductance displays a plateau in the Coulomb valleys, hinting at a crossover to the topological Kondo regime.

Our results are obtained through a MPS approach that allows for the study of topological Kondo models without recurring to perturbation theory in the Majorana-lead coupling nor requiring any particular hierarchy of the involved energy scales as expected in realistic devices [19]. It is therefore well suited to understand the crossover

between strong and weak-coupling regimes as well as the corrections to the RG predictions on the TKE when we probe the system at energy scales comparable with T_K .

Our method can be extended to more complex topological Kondo models, including the coupling of Majorana modes [9] caused by crossed-Andreev and cotunneling processes, the generalization to multichannel topological systems [] and the presence of spurious quantum dots in the devices, which may cause additional Kondo effects [50–54]. This approach can be applied to the transport features of many strongly interacting nanodevices based on quantum dots coupled to superconducting islands[55–58]. Our method can be extended to more complex topological Kondo models, including the coupling of Majorana modes [9] caused by crossed-Andreev and cotunneling processes, the generalization to multichannel topological systems [] and the presence of spurious quantum dots in the devices, which may cause additional Kondo effects [50–54]. This approach can be applied to the transport features of many strongly interacting nanodevices based on quantum dots coupled to superconducting islands[55–58]. Our method can be extended to more complex topological Kondo models, including the coupling of Majorana modes [9] caused by crossed-Andreev and cotunneling processes, the generalization to multichannel systems [59, 60] and the presence of spurious quantum dots in the devices, which may cause additional Kondo effects [50–54]. This approach can be applied to the transport features of many strongly interacting nanodevices based on quantum dots coupled to superconducting islands [55–58].

ACKNOWLEDGMENTS

e. Acknowledgements.- We thank F. Bucchieri, R. Egger and J. Paaske for insightful discussions. M.W., L.M., and M.B. are supported by the Villum Foundation (Research Grant No. 25310). C.-M.C. acknowledges the support by the Ministry of Science and Technology (MOST) under Grant No. 111-2112-M-110-006-MY3, and by the Yushan Young Scholar Program under the Ministry of Education (MOE) in Taiwan. This project has received funding from the European Union’s Horizon 2020 research and innovation program under the Marie Skłodowska-Curie Grant Agreement No. 847523 “INTERACTIONS.” This work was supported by Q@TN, the joint lab between University of Trento, FBK—Fondazione Bruno Kessler, INFN—National Institute for Nuclear Physics, and CNR—National Research Council.

[1] E. Prada, P. San-Jose, M. W. de Moor, A. Geresdi, E. J. Lee, J. Klinovaja, D. Loss, J. Nygård, R. Aguado,

and L. P. Kouwenhoven, From andreev to majorana bound states in hybrid superconductor–semiconductor

- nanowires, *Nature Reviews Physics* **2**, 575 (2020).
- [2] C. W. J. Beenakker, Search for non-Abelian Majorana braiding statistics in superconductors, *SciPost Phys. Lect. Notes*, 15 (2020).
 - [3] K. Flensberg, F. von Oppen, and A. Stern, Engineered platforms for topological superconductivity and majorana zero modes, *Nature Reviews Materials* **6**, 944 (2021).
 - [4] B. Béri and N. R. Cooper, Topological Kondo effect with Majorana fermions, *Phys. Rev. Lett.* **109**, 156803 (2012).
 - [5] B. Béri, Majorana-Klein hybridization in topological superconductor junctions, *Phys. Rev. Lett.* **110**, 216803 (2013).
 - [6] A. Altland and R. Egger, Multiterminal Coulomb-Majorana junction, *Phys. Rev. Lett.* **110**, 196401 (2013).
 - [7] D. Liu, Z. Cao, X. Liu, H. Zhang, and D. E. Liu, Topological kondo device for distinguishing quasi-majorana and majorana signatures, *Phys. Rev. B* **104**, 205125 (2021).
 - [8] K. Michaeli, L. A. Landau, E. Sela, and L. Fu, Electron teleportation and statistical transmutation in multiterminal Majorana islands, *Phys. Rev. B* **96**, 205403 (2017).
 - [9] A. Altland, B. Béri, R. Egger, and A. M. Tsvelik, Multichannel Kondo impurity dynamics in a Majorana device, *Phys. Rev. Lett.* **113**, 076401 (2014).
 - [10] M. R. Galpin, A. K. Mitchell, J. Temaismithi, D. E. Logan, B. Béri, and N. R. Cooper, Conductance fingerprint of majorana fermions in the topological kondo effect, *Phys. Rev. B* **89**, 045143 (2014).
 - [11] L. Herviou, K. Le Hur, and C. Mora, Many-terminal Majorana island: From topological to multichannel Kondo model, *Phys. Rev. B* **94**, 235102 (2016).
 - [12] F. Buccheri, A. Nava, R. Egger, P. Sodano, and D. Giuliano, Violation of the wiedemann-franz law in the topological kondo model, *Phys. Rev. B* **105**, L081403 (2022).
 - [13] A. Altland, B. Béri, R. Egger, and A. M. Tsvelik, Bethe ansatz solution of the topological Kondo model, *J. Phys. A: Math. Theor.* **47**, 265001 (2014).
 - [14] F. Buccheri, H. Babujian, V. E. Korepin, P. Sodano, and A. Trombettoni, Thermodynamics of the topological Kondo model, *Nucl. Phys. B* **896**, 52 (2015).
 - [15] B. Béri, Exact nonequilibrium transport in the topological Kondo effect, *Phys. Rev. Lett.* **119**, 027701 (2017).
 - [16] M. Papaj, Z. Zhu, and L. Fu, Multichannel charge Kondo effect and non-Fermi-liquid fixed points in conventional and topological superconductor islands, *Phys. Rev. B* **99**, 014512 (2019).
 - [17] C.-M. Chung, M. M. Wauters, and M. Burrello, Matrix product state simulations of quantum quenches and transport in coulomb blockaded superconducting devices, *Phys. Rev. B* **106**, 094308 (2022).
 - [18] T. Kanne, D. Olsteins, M. Marnauza, A. Vekris, J. C. Estrada Saldaña, S. Loric, R. D. Schlosser, D. Ross, S. Csonka, K. Grove-Rasmussen, and J. Nygård, Double nanowires for hybrid quantum devices, *Advanced Functional Materials* **32**, 2107926 (2022).
 - [19] A. Vekris, J. C. Estrada Saldaña, T. Kanne, T. Hvid-Olsen, M. Marnauza, D. Olsteins, M. M. Wauters, M. Burrello, J. Nygård, and K. Grove-Rasmussen, Electronic transport in double-nanowire superconducting islands with multiple terminals, *Nano Letters* **22**, 5765 (2022), pMID: 35833741, <https://doi.org/10.1021/acs.nanolett.2c01161>.
 - [20] Y. Oreg, G. Refael, and F. von Oppen, Helical liquids and majorana bound states in quantum wires, *Phys. Rev. Lett.* **105**, 177002 (2010).
 - [21] R. M. Lutchyn, J. D. Sau, and S. Das Sarma, Majorana fermions and a topological phase transition in semiconductor-superconductor heterostructures, *Phys. Rev. Lett.* **105**, 077001 (2010).
 - [22] K. Grove-Rasmussen, G. Steffensen, A. Jellinggaard, M. H. Madsen, R. Žitko, J. Paaske, and J. Nygård, Yu–Shiba–Rusinov screening of spins in double quantum dots, *Nature Communications* **9**, 2376 (2018).
 - [23] S. Vaitiekėnas, R. S. Souto, Y. Liu, P. Krogstrup, K. Flensberg, M. Leijnse, and C. M. Marcus, Evidence for spin-polarized bound states in semiconductor–superconductor–ferromagnetic-insulator islands, *Phys. Rev. B* **105**, L041304 (2022).
 - [24] R. S. Souto, M. M. Wauters, K. Flensberg, M. Leijnse, and M. Burrello, Multiterminal transport spectroscopy of subgap states in coulomb-blockaded superconductors, *Phys. Rev. B* **106**, 235425 (2022).
 - [25] B. van Heck, A. R. Akhmerov, F. Hassler, M. Burrello, and C. W. J. Beenakker, Coulomb-assisted braiding of Majorana fermions in a Josephson junction array, *New J. Phys.* **14**, 035019 (2012).
 - [26] S. Plugge, A. Rasmussen, R. Egger, and K. Flensberg, Majorana box qubits, *New J. Phys.* **19**, 012001 (2017).
 - [27] See supplemental material for further data and technical details..
 - [28] K. G. Wilson, The renormalization group: Critical phenomena and the Kondo problem, *Rev. Mod. Phys.* **47**, 773 (1975).
 - [29] L. G. G. V. Dias da Silva, F. Heidrich-Meisner, A. E. Feiguin, C. A. Büsser, G. B. Martins, E. V. Anda, and E. Dagotto, Transport properties and Kondo correlations in nanostructures: Time-dependent DMRG method applied to quantum dots coupled to Wilson chains, *Phys. Rev. B* **78**, 195317 (2008).
 - [30] M. M. Wauters, C.-M. Chung, L. Maffi, and M. Burrello, Simulations of the dynamics of quantum impurity problems with matrix product states (2023), [arXiv:2304.13756](https://arxiv.org/abs/2304.13756) [cond-mat.str-el].
 - [31] A. Keselman, C. Murthy, B. van Heck, and B. Bauer, Spectral response of Josephson junctions with low-energy quasiparticles, *SciPost Phys.* **7**, 50 (2019).
 - [32] J. Haegeman, J. I. Cirac, T. J. Osborne, I. Pižorn, H. Verschelde, and F. Verstraete, Time-dependent variational principle for quantum lattices, *Phys. Rev. Lett.* **107**, 070601 (2011).
 - [33] J. Haegeman, C. Lubich, I. Oseledets, B. Vandereycken, and F. Verstraete, Unifying time evolution and optimization with matrix product states, *Phys. Rev. B* **94**, 165116 (2016).
 - [34] M. Yang and S. R. White, Time-dependent variational principle with ancillary Krylov subspace, *Phys. Rev. B* **102**, 094315 (2020).
 - [35] M. Fishman, S. R. White, and E. M. Stoudenmire, The ITensor Software Library for Tensor Network Calculations, *SciPost Phys. Codebases*, 4 (2022).
 - [36] The source code can be found in the repository <https://github.com/chiamin/QuenchTransportTwoChains>.
 - [37] D. Lobaskin and S. Kehrein, Crossover from nonequilibrium to equilibrium behavior in the time-dependent kondo model, *Phys. Rev. B* **71**, 193303 (2005).
 - [38] F. B. Anders and A. Schiller, Real-time dynamics in quantum-impurity systems: A time-dependent numerical renormalization-group approach, *Phys. Rev. Lett.* **95**,

- 196801 (2005).
- [39] M. F. Cavalcante, R. G. Pereira, and M. C. O. Aguiar, Quench dynamics of the kondo effect: Transport across an impurity coupled to interacting wires, *Phys. Rev. B* **107**, 075110 (2023).
- [40] E. H. Lieb and D. W. Robinson, The finite group velocity of quantum spin systems, *Commun. Math. Phys.* **28**, 251 (1972).
- [41] L. Bonnes, F. H. L. Essler, and A. M. Läuchli, “light-cone” dynamics after quantum quenches in spin chains, *Phys. Rev. Lett.* **113**, 187203 (2014).
- [42] B. Bertini, M. Collura, J. De Nardis, and M. Fagotti, Transport in out-of-equilibrium xxz chains: Exact profiles of charges and currents, *Phys. Rev. Lett.* **117**, 207201 (2016).
- [43] J. Viti, J.-M. Stéphan, J. Dubail, and M. Haque, Inhomogeneous quenches in a free fermionic chain: Exact results, *EPL (Europhysics Letters)* **115**, 40011 (2016).
- [44] F. H. L. Essler and M. Fagotti, Quench dynamics and relaxation in isolated integrable quantum spin chains, *Journal of Statistical Mechanics: Theory and Experiment* **2016**, 064002 (2016).
- [45] M. Ljubotina, S. Sotiriadis, and T. Prosen, Non-equilibrium quantum transport in presence of a defect: the non-interacting case, *SciPost Phys.* **6**, 4 (2019).
- [46] J. I. Väyrynen, A. E. Feiguin, and R. M. Lutchyn, Signatures of topological ground state degeneracy in majorana islands, *Phys. Rev. Res.* **2**, 043228 (2020).
- [47] The simulations with $M = 3$ are performed by setting $J_2 = 0$.
- [48] Z. He and A. J. Millis, Entanglement entropy and computational complexity of the Anderson impurity model out of equilibrium: Quench dynamics, *Phys. Rev. B* **96**, 085107 (2017).
- [49] A. Zazunov, A. Altland, and R. Egger, Transport properties of the Coulomb–Majorana junction, *New J. Phys.* **16**, 015010 (2014).
- [50] M. Cheng, M. Becker, B. Bauer, and R. M. Lutchyn, Interplay between Kondo and Majorana interactions in quantum dots, *Phys. Rev. X* **4**, 031051 (2014).
- [51] R. López, M. Lee, L. m. c. Serra, and J. S. Lim, Thermoelectrical detection of Majorana states, *Phys. Rev. B* **89**, 205418 (2014).
- [52] J. F. Silva, L. G. G. V. D. da Silva, and E. Vernek, Robustness of the Kondo effect in a quantum dot coupled to Majorana zero modes, *Phys. Rev. B* **101**, 075428 (2020).
- [53] I. Weymann, K. P. Wójcik, and P. Majek, Majorana-Kondo interplay in T-shaped double quantum dots, *Phys. Rev. B* **101**, 235404 (2020).
- [54] A. E. Svetogorov, D. Loss, and J. Klinovaja, Enhancement of the Kondo effect in a quantum dot formed in a full-shell nanowire, *Phys. Rev. B* **107**, 134505 (2023).
- [55] C.-X. Liu, G. Wang, T. Dvir, and M. Wimmer, Tunable superconducting coupling of quantum dots via Andreev bound states in semiconductor-superconductor nanowires, *Phys. Rev. Lett.* **129**, 267701 (2022).
- [56] A. Tsintzis, R. S. Souto, and M. Leijnse, Creating and detecting poor man’s Majorana bound states in interacting quantum dots, *Phys. Rev. B* **106**, L201404 (2022).
- [57] T. Dvir, G. Wang, N. van Loo, C.-X. Liu, G. P. Mazur, A. Bordin, S. L. D. Ten Haaf, J.-Y. Wang, D. van Driel, F. Zatelli, X. Li, F. K. Malinowski, S. Gazibegovic, G. Badawy, E. P. A. M. Bakkers, M. Wimmer, and L. P. Kouwenhoven, Realization of a minimal Kitaev chain in coupled quantum dots, *Nature* **614**, 445 (2023).
- [58] A. Tsintzis, R. S. Souto, K. Flensberg, J. Danon, and M. Leijnse, Roadmap towards Majorana qubits and non-abelian physics in quantum dot-based minimal Kitaev chains (2023), arXiv:2306.16289 [cond-mat.mes-hall].
- [59] I. Affleck and D. Giuliano, Topological superconductor–luttinger liquid junctions, *Journal of Statistical Mechanics: Theory and Experiment* **2013**, P06011 (2013).
- [60] G. Li, Y. Oreg, and J. I. Väyrynen, Multichannel topological kondo effect, *Phys. Rev. Lett.* **130**, 066302 (2023).
- [61] D. Sticlet, C. Bena, and P. Simon, *Phys. Rev. Lett.* **108**, 096802 (2012), URL <https://link.aps.org/doi/10.1103/PhysRevLett.108.096802>.
- [62] M. Kjaergaard, K. Wölms, and K. Flensberg, *Phys. Rev. B* **85**, 020503 (2012), URL <https://link.aps.org/doi/10.1103/PhysRevB.85.020503>.
- [63] M. M. Rams and M. Zwolak, *Phys. Rev. Lett.* **124**, 137701 (2020), URL <https://link.aps.org/doi/10.1103/PhysRevLett.124.137701>.
- [64] B. van Heck, R. M. Lutchyn, and L. I. Glazman, *Phys. Rev. B* **93**, 235431 (2016), URL <https://link.aps.org/doi/10.1103/PhysRevB.93.235431>.
- [65] M. Yoshida, M. A. Whitaker, and L. N. Oliveira, *Phys. Rev. B* **41**, 9403 (1990), URL <https://link.aps.org/doi/10.1103/PhysRevB.41.9403>.
- [66] I. Affleck, *Nucl. Phys. B* **336**, 517 (1990), ISSN 0550-3213.
- [67] I. Affleck and A. W. W. Ludwig, *Nucl. Phys. B* **360**, 641 (1991), ISSN 0550-3213.

SUPPLEMENTAL MATERIALS

I. MINIMAL TWO-SITES KITAEV CHAIN DESCRIPTION

In this Section we review the minimal double-nanowire description we use for modelling each nanowire and its comparison with standard constructions adopted to describe the topological Kondo effect.

The Majorana modes appearing in nanowire models that include spin-orbit and Zeeman coupling are characterized in general by a spinful wavefunction with position-dependent spinors [61, 62]. Therefore, a general tunnelling term combining these Majorana modes with spinful external leads couples them with a single related spin polarization; lead electrons in the orthogonal spin component, instead, are coupled by tunneling only to high energy states beyond the gap of the superconducting system. This justifies the spinless approximation that we adopt in our model, since, in the low-energy sector, Majorana modes interact with a single fermionic species.

Differently from all previous investigations of the topological Kondo effect, we consider a minimal model that includes also Bogoliubov excitations and can be regarded as an effective zero-bandwidth description of the two superconducting nanowires. This minimal model corresponds to a two-site Kitaev chain for each nanowire. It should be noted that this model can be extended for longer chains. The Hamiltonian for the chain $\sigma = \uparrow, \downarrow$ is given by:

$$\widehat{H}_{\text{kit}}^{(\sigma)} = \sum_{j=1}^2 \left[-\mu_{\text{sys}} \hat{d}_{j,\sigma}^\dagger \hat{d}_{j,\sigma} + \left(-t_{\text{sys}} \hat{d}_{j+1,\sigma}^\dagger \hat{d}_{j,\sigma} + \Delta_P e^{i\Phi} \hat{d}_{j+1,\sigma} \hat{d}_{j,\sigma} + \text{H.c.} \right) \right], \quad (7)$$

where the index j labels the site and Φ is the superconducting phase of the aluminum backbone. In our simulations, we set $t_{\text{sys}} = \Delta_P = 0.5t_0$ and $\mu_{\text{sys}} = 0.01t_0$ to avoid a perfect degeneracy of the states. The resulting energy splitting of the MZMs, however, is of order $10^{-4}t_0$ and is the smallest energy scale in our system. Before constructing the MPS representation of the full system, we diagonalize the quadratic Hamiltonians in Equation (7) and define the quasiparticle excitations.

For simplicity, in the following, we consider only the upper chain, as the two chains are indistinguishable at equilibrium.

The physics of the MZMs is manifest by expressing each fermionic operator in terms of two Majorana fermions. In the case of the upper wire, we define:

$$\hat{d}_{j,\uparrow} = \frac{e^{-i\Phi/2}}{2} \left(\hat{\gamma}_{j,B} - i\hat{\gamma}_{j,A} \right) \quad (8)$$

as schematically represented in Fig. 6. We consider the limit with $\mu_{\text{sys}} = 0$ and $\Delta_P = t_{\text{sys}}$, such that the Hamiltonian is given by $\widehat{H}_{\text{kit}}^{(\uparrow)} = -i\Delta_P \hat{\gamma}_{2,A} \hat{\gamma}_{1,B}$ and couples Majorana fermions only at adjacent lattice sites (Fig. 6). The ends of the chain support the unpaired MZMs $\hat{\gamma}_1 = \hat{\gamma}_{1,A}$ and $\hat{\gamma}_2 = \hat{\gamma}_{2,B}$ which allow us to define the zero-energy quasiparticle operator $\hat{f}_{0,\uparrow}$ introduced in the main text. In the quasiparticle basis, the first excited state has energy $\epsilon_{1,\uparrow} = 2\Delta_P$ and corresponds to the operator $\hat{f}_{1,\uparrow} = (\hat{\gamma}_{2,A} - i\hat{\gamma}_{1,B})/2$, such that the Hamiltonian can be written as

$$\widehat{H}_{\text{Kit}}^{(\uparrow)} = 2\Delta_P \left(\hat{f}_{1,\uparrow}^\dagger \hat{f}_{1,\uparrow} - 1/2 \right). \quad (9)$$

The same construction is valid for the lower chain.

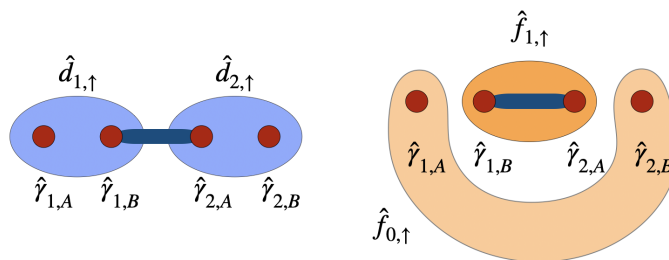


Figure 6. Each fermionic site of the Kitaev chain can be decomposed in two Majorana operators to make the MZMs physics more transparent. Quasiparticles states are represented schematically on the right. The thick blue link represents the interaction in Eq. (9).

To illustrate the relation of our construction with the standard models adopted for the description of the topological Kondo effect, we can consider the ideal topological limit with $\mu_{\text{sys}} = 0$, and restrict the model we analyzed to its low-energy sector. The resulting effective coupling between the four Majorana zero-modes and the lead fermions is given by:

$$\hat{H}_{t,0} = - \sum_{\alpha=1}^4 \frac{iJ_{\alpha}}{2} \hat{\gamma}_{\alpha} \left(\hat{c}_{\alpha,1} e^{i\Phi/2} + \hat{c}_{\alpha,1}^{\dagger} e^{-i\Phi/2} \right). \quad (10)$$

This effective tunneling Hamiltonian corresponds to the coupling adopted in Refs. [5, 6] (with discretized lead degrees of freedom) to derive the topological Kondo effect. Away from the charge degeneracy point, by treating $\hat{H}_{t,0}$ as a perturbation of the charging energy interaction in \hat{H}_{sys} , one obtains the effective topological Kondo Hamiltonian term, quadratic in the Majorana modes, studied, for instance, in Ref. [4]:

$$\hat{H}_{\text{eff}} = \sum_{\alpha \neq \beta} \lambda_{\alpha\beta}^{+} \hat{\gamma}_{\alpha} \hat{\gamma}_{\beta} \hat{c}_{\alpha,1}^{\dagger} \hat{c}_{\beta,1} - \sum_{\alpha} \lambda_{\alpha\alpha}^{-} \hat{c}_{\alpha,1}^{\dagger} \hat{c}_{\alpha,1} \quad (11)$$

where $\lambda_{\alpha\beta}^{\pm} = \frac{J_{\alpha} J_{\beta}}{4} \left(\frac{1}{2E_C |n_g - 1/2|} \pm \frac{1}{2E_C |n_g + 1/2|} \right)$ for $0 < n_g < 1$ and n_g sufficiently far from $1/2$. The Majorana binomials in Eq. (11) define the effective Majorana magnetization in the three directions. Therefore, \hat{H}_{eff} can be recast in an anisotropic Kondo model. This mapping was adopted in Ref. [10] to study the TKE in the axial symmetric limit $J_1 = J_2$ through NRG techniques.

II. THE MATRIX PRODUCT STATE CONSTRUCTION

A. Auxiliary charge site

In order to simulate the topological Kondo model, we need to account for both its superconducting pairing and the charging energy of the Cooper-pair box. Importantly, the mean field BCS description of the superconducting system does not preserve the total particle number, but only its parity. This means that we cannot deduce the total charge of the Cooper-pair box \hat{N} directly from the quasiparticle MPS construction. In order to overcome this problem we add an independent auxiliary charge site to the tensor network representation to keep track of the charge and its dynamics [17, 31].

First of all, one can promote the SC phase $e^{-i\Phi/2}$ in (8) as the operator $e^{-i\hat{\Phi}/2}$ which lowers the number of electrons on the box by one (due to the charge phase relation $[\hat{N}, \hat{\Phi}] = -2i$). In this way, the decomposition in Eq. (8) enables to separate this charge degree of freedom from the quasiparticle number. We can therefore describe charge dynamics by adding to our MPS an auxiliary site whose local Hilbert space is spanned by the eigenstates $|N\rangle$ of the charge \hat{N} [17].

The tunneling Hamiltonian \hat{H}_t becomes the sum of three-site operators of the form:

$$\hat{H}_t = - \sum_{\alpha=1}^4 \sum_{\sigma,n} J_{\alpha} \left[e^{i\hat{\Phi}/2} \left(u_{\alpha,\sigma,n} \hat{f}_{\sigma,n}^{\dagger} + v_{\alpha,\sigma,n} \hat{f}_{\sigma,n} \right) \hat{c}_{\alpha,1} + \text{H.c.} \right]. \quad (12)$$

where the operator $e^{\pm i\hat{\Phi}/2}$ acts on the auxiliary site and raises/lowers the charge eigenvalue N . Finally, charging energy costs are straightforwardly taken into account by considering the state of the auxiliary site, via $\hat{H}_c = E_c \left(\hat{N} - n_g \right)^2$ in Eq. (1) in the main text.

The auxiliary charge site construction is numerically implemented by restricting its local Hilbert, $N \in [-N_{\text{max}}, N_{\text{max}}]$, with $N_{\text{max}} = 5$ (such that $e^{\pm i\hat{\Phi}/2}$ are represented as 11×11 matrices). Moreover, to remove the redundancy introduced by the auxiliary site, we constrain the parity of \hat{N} to be the same as the parity of the total occupation of the quasiparticle states in the Majorana Cooper-pair box [17]. Namely, once defining the operator

$$\hat{P} = (-1)^{\hat{N} + \sum_{n,\sigma} \hat{f}_{n,\sigma}^{\dagger} \hat{f}_{n,\sigma}}, \quad (13)$$

the following relation

$$\hat{P} |\psi_{\text{phys}}\rangle = |\psi_{\text{phys}}\rangle, \quad (14)$$

has to be valid for any physical states $|\psi_{\text{phys}}\rangle$. Our MPS and matrix product operator construction encodes such \mathbb{Z}_2 constraint.

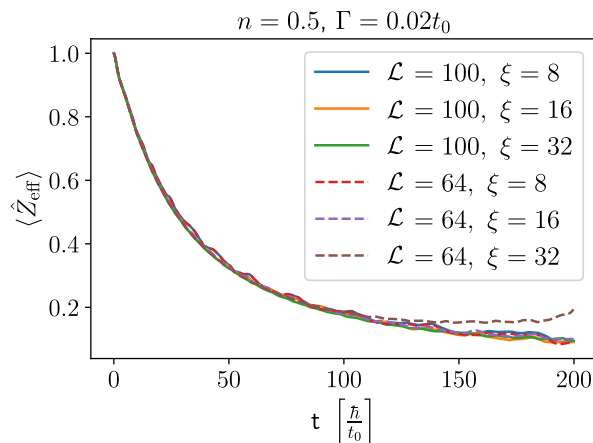


Figure 7. Relaxation of the effective magnetization at the charge degeneracy point for different combinations of lead length \mathcal{L} and hopping decay length ξ .

B. TDVP Dynamics and transport quantities

We simulate the dynamics of the system through the TDVP algorithm, which is not limited by the long-range Hamiltonian resulting from the energy basis choice for the MPS. The Hamiltonian \hat{H} is represented as a matrix product operator of maximum bond dimension $\chi = 16$.

A crucial element of our simulation is the exponential decay of the hopping amplitude inside the leads. It allows for both a tunable energy resolution at small bias and for simulating an effectively longer system by slowing down the current as it propagates in the leads [17]. To ensure that we get physical results, a first step in our simulations is to verify the convergence of the dynamics with respect to the lead length \mathcal{L} and the hopping decay length ξ . We report in Fig. 7 an example of such calculation, where we plot the effective magnetization as function of time for different choices of \mathcal{L} and ξ . Beside the combination $\xi = 32, \mathcal{L} = 64$, all other curves collapse perfectly on each other, showing that the simulations are converged to a physically meaningful dynamics. The deviation from the physical behaviour is expected to take place at $t_{\text{max}} \simeq \frac{\hbar}{t_0} \frac{\xi}{2} (e^{\mathcal{L}/\xi} - 1)$ [17], which is approximately $100\hbar/t_0$ for $\mathcal{L} = 64, \xi = 32$, as confirmed by the simulations.

Once convergence is ensured, \mathcal{L} and ξ are chosen in such a way that the current signal displays a long enough plateau for $t < t_{\text{max}}$. When these conditions are met, we can characterize the emerging non-equilibrium quasi-steady states, that provide faithful descriptions of the physical behavior of the (infinite) system in its stationary state (see, for instance, Refs. [42, 44]). An example of the current after the quench is depicted in Fig. 8(a). To extract the values of the currents analyzed in the main text, we average the signal after it reaches the stationary value and estimate the errorbars through standard binning techniques.

Thanks to the chosen basis, after the quantum quench, the entanglement entropy of the system increases logarithmically with time [17, 63] and it is mainly localized in an energy window proportional to the voltage bias. Outside that window, the entanglement entropy is mostly time-independent, as we show in Fig. 8(b) and (c). See Ref. [17] for more details about the MPS construction and dynamics.

We finally observe that the Hamiltonian we adopt to describe the double-nanowire model displays an additional symmetry with respect to the most common topological Kondo models [4–6]. Indeed, the dynamics we analyze separately preserves the two fermionic parities:

$$\hat{P}_{\uparrow} = (-1)^{\sum_{\alpha=1,2} \sum_{l=1}^{\mathcal{L}} \hat{c}_{\alpha,l}^{\dagger} \hat{c}_{\alpha,l} + \sum_{n=0,1} \hat{f}_{n,\uparrow}^{\dagger} \hat{f}_{n,\uparrow}}, \quad (15)$$

$$\hat{P}_{\downarrow} = (-1)^{\sum_{\alpha=3,4} \sum_{l=1}^{\mathcal{L}} \hat{c}_{\alpha,l}^{\dagger} \hat{c}_{\alpha,l} + \sum_{n=0,1} \hat{f}_{n,\downarrow}^{\dagger} \hat{f}_{n,\downarrow}}. \quad (16)$$

These symmetries reflect the fact that we are neglecting crossed-Andreev and direct cotunneling processes mediated by the superconducting island between the two nanowires. These conservations have the important effect of breaking the particle-hole-like symmetry of the dynamics between systems characterized by n_g and $1 - n_g$, as can be seen from Fig. 5 in the main text at large coupling. The initial ground states $|00\rangle$ ($N = 0$) for $n_g < 0.5$ and $|10\rangle$ ($N = 1$) for $n_g > 0.5$ correspond to different sectors of \hat{P}_{\downarrow} and are not mapped one into the other by the symmetry.

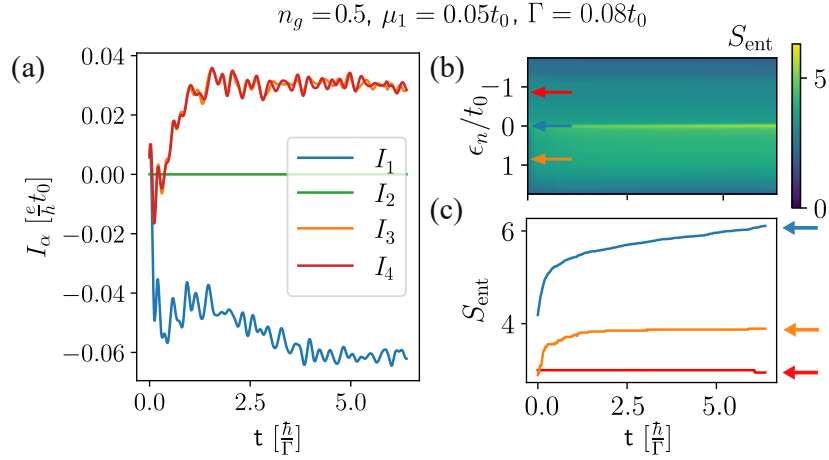


Figure 8. Typical dynamics of the current and entanglement entropy after a quantum quench for a three-terminal device. (a) Time dependence of the current on each lead. I_1 has a negative sign because it is the only in-going current. $I_2 = 0$ because the corresponding lead is decoupled from the device. (b) Entanglement entropy at each bond of the MPS as a function of energy and time. The three arrows mark the horizontal line cuts corresponding to the curves shown in panel (c). Simulation parameters: $\mathcal{L} = 100$, $\xi = 32$.

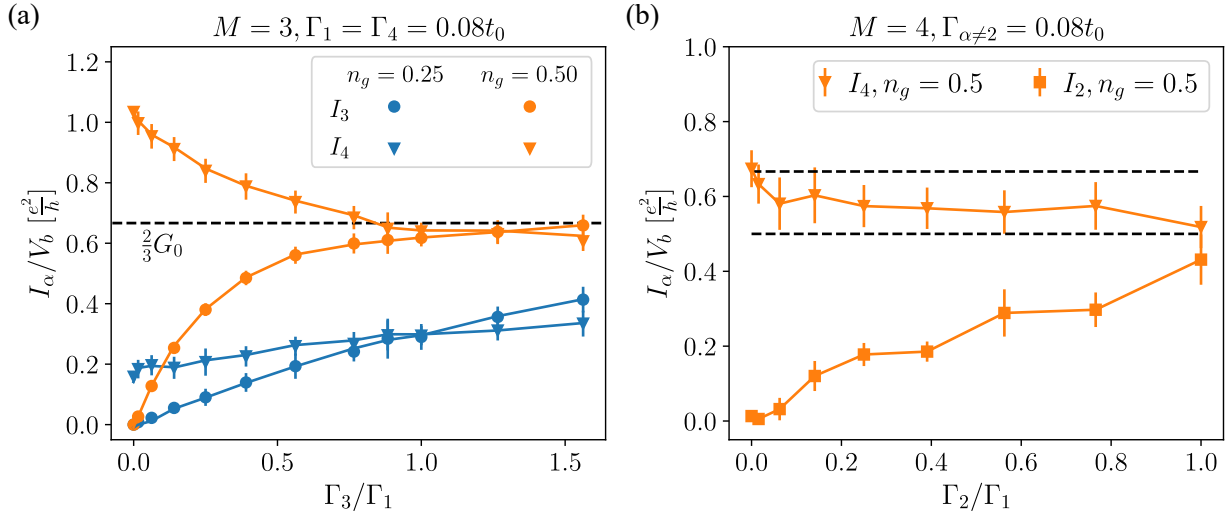


Figure 9. (a) Nonlocal current as a function of the varying coupling strength Γ_3 , at the charge degeneracy point $n_g = 0.5$ and in the even valley $n_g = 0.25$. Lead 2 is uncoupled ($\Gamma_2 = 0$). (b) Nonlocal currents as a function of the varying coupling strength Γ_2 , at the charge degeneracy point $n_g = 0.5$. The two horizontal dashed lines mark $G = \frac{2}{M}G_0$ for $M = 3, 4$. In both panels $E_c = 0.4$, $eV_b = 0.01t_0$, $L = 100$, and $\xi = 32$.

III. FURTHER TRANSPORT RESULTS

A. Asymmetric couplings

Here we investigate the effect of introducing an asymmetry in the couplings Γ_α on the transport properties.

We first analyze a device with three leads ($\Gamma_2 = 0$), where two of them have the same coupling strength $\Gamma_1 = \Gamma_4 = 0.08t_0$, which corresponds to the strong coupling regime explored in the main text, while the third is varied. In Fig. 9(a) we plot the nonlocal currents I_3 and I_4 divided by the bias on lead 1 as we vary $\Gamma_3 \in [0, 1.6\Gamma_1]$. At the charge degeneracy point (orange symbols), the data suggest that the current is approximately stable for a broad range of couplings $\Gamma_3 \gtrsim \Gamma_1$, and, within the error bars, is compatible with the linear conductance associated to the TKE (horizontal dashed line). As Γ_3 decreases, I_3 also decreases and vanishes when the lead is finally decoupled from the system. At the same time, I_4 increases and approaches the quantized value $I_4 = G_0V_b$ when the device has only two

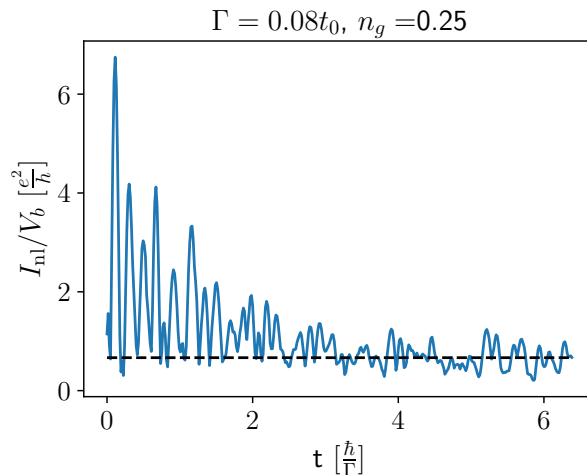


Figure 10. Time dependence of the nonlocal current for $M = 3$ and $n_g = 0.25$, averaged over 4 values of $\xi = 2, 4, 8, 16$. The chosen bias is $eV_b = 0.001t_0$. The horizontal dashed line marks the TKE prediction.

terminals, as we expect from the resonant tunneling mediated by MZMs with symmetric couplings [17, 64]. As we move deeper in the Coulomb valley ($n_g = 0.25$, blue symbols), the system appears to be further away from the TKE regime and the current shows a roughly linear dependence on Γ_3 . Interestingly, however, the current I_4 decreases upon switching off Γ_3 , despite keeping Γ_4 constant. This is in contrast with the single resonant level prediction of Eq. (17), confirming that a contribution to the current originating from a strongly coupled state is present also in the Coulomb valleys, even though the TKE quantization of the conductance is not recovered for the chosen parameter ranges.

Let us now focus on the crossover between $M = 4$ and $M = 3$: we consider a four-terminal device where we tune the coupling Γ_2 from the symmetric configuration, $\Gamma_\alpha = 0.08t_0$ on any lead, to $\Gamma_2 = 0$, while keeping a small voltage bias $eV_b = 0.01t_0$ on lead 1. In Fig. 9(b) we show the nonlocal currents I_2 and I_4 for $n_g = 0.5$, where the Kondo temperature is maximal, as we switch off Γ_2 . When $\Gamma_2 = \Gamma_1$, the current on both leads is again compatible with the TKE prediction with $M = 4$ (lower horizontal dashed line). As Γ_2 decreases, I_2 and I_4 display opposite behaviors; the former decreases and vanishes following Γ_2 while the latter displays first a rather flat plateau followed by a rapid increase to match the TKE prediction for $M = 3$ when $\Gamma_2 \rightarrow 0$ (higher horizontal dashed line). The current on lead 3 (data not shown) follows closely the signal on I_4 .

B. Low bias transport

Transport simulations at very low bias are hampered by a low signal-to-noise ratio that prevents from an accurate estimate of the average current in the nonequilibrium quasi-steady state. This limitation is relevant for low Kondo temperatures as, for instance, in the Coulomb valleys. To partially circumvent this issue, inspired by the so-called z-trick [65] commonly used in NRG methods, here we consider data obtained by averaging over different logarithmic discretizations of the energy levels of the leads. In particular, we average the currents over different decay lengths of the hopping amplitude in the leads. In Fig. 10 we plot an example of this procedure: we consider $n_g = 0.25$ (even-parity Coulomb valley), $E_c = 0.4t_0$, $M = 3$, and $\Gamma = 0.08t_0$. The corresponding Kondo temperature extracted from the magnetization dynamics is $T_K \sim 0.01t_0$, see Fig. 3(c) of the main text. To capture the transport signature of the TKE, we perform different simulations with a small bias $eV_b = 10^{-3}t_0$ on lead 1 and $\xi = \{2, 4, 8, 16\}$. We then average the outgoing current over the different values of ξ . This reduces the amplitude of the current oscillations, and leads to a good match with the TKE prediction $G_{\text{TKE}} = \frac{2}{M}G_0$ also in the Coulomb valleys.

In the main text, we compare the extracted low bias conductance with the resonant level approximation. This consists in one single charge degree of freedom \hat{n} affected by a charging energy $E_c (\hat{n} - n_g)^2$ and coupled with M leads with symmetric tunneling rates $\Gamma_\alpha = \Gamma$. For a finite bias difference μ between leads, the non-local conductance is given by

$$G_{\text{RL}}(n_g, \mu) = \frac{e^2}{h} \frac{4\Gamma^2}{M^2\Gamma^2 + 4[\mu - E_c(1 - 2n_g)]^2}. \quad (17)$$

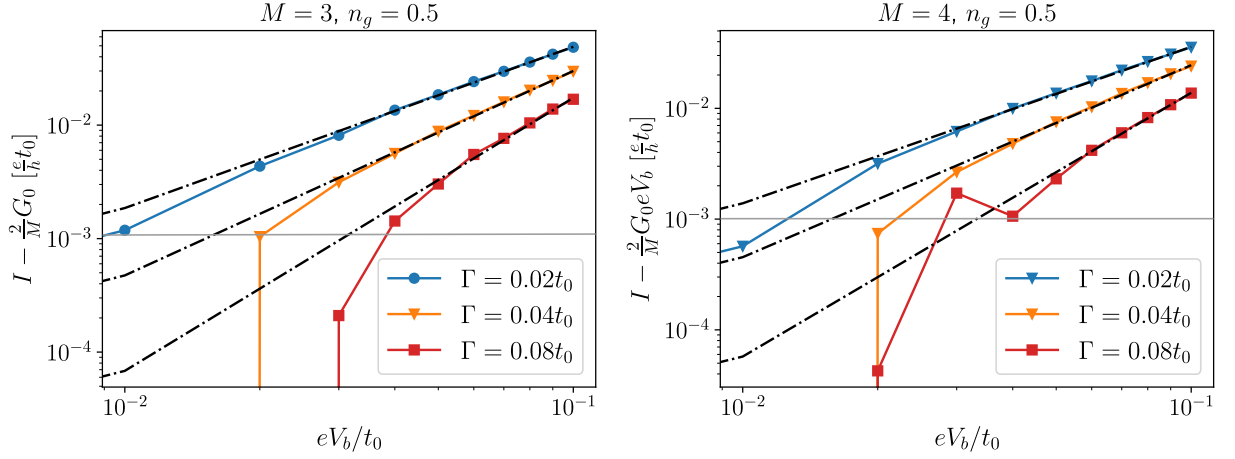


Figure 11. Deviation of the average non-local current from the linear regime $I = \frac{2}{M}G_0V_b$, for $M = 3, 4$, $n_g = 0.5$ and $E_c = 0.4t_0$. The black dashed lines are power-law fits bx^a of the data. The values of a for $M = 3$ are 1.42(1) ($\Gamma = 0.02t_0$), 1.80(1) ($\Gamma = 0.04t_0$), and 2.41(3) ($\Gamma = 0.08t_0$), while for $M = 4$ we obtain 1.41(2) ($\Gamma = 0.02t_0$), 1.73(2) ($\Gamma = 0.04t_0$), and 2.38(4) ($\Gamma = 0.08t_0$). The grey line indicates the numerical precision.

This approximation gives the corresponding dashed lines plotted in Fig. 5 of the main text, for different values of the tunneling rate.

C. Finite bias corrections

Finally, we discuss the finite bias corrections to the currents close to TKE linear response behaviour, $I = \frac{2}{M}G_0V_b$. In a renormalization group sense, a power law correction $G = 2G_0/M - AV_b^\alpha$ is related to the scaling dimension of the most relevant operator which arises at the TKE fixed point. In particular, a fixed point described by the Fermi liquid (FL) theory displays a quadratic correction for the conductance ($\alpha = 2$). The topological Kondo effect, instead, is predicted to display non-Fermi liquid corrections defined by the universal fractional exponent $\alpha = 2(1 - 2/M)$ [11, 15, 49]. The boundary CFT approach [66, 67] (adapted to the $SO(M)$ case) can also provide a full description of the scaling of these perturbations close to the strong-coupling fixed point. Additionally, techniques based on the mapping on boundary sine-Gordon models have been adopted to study the universal features of the transport at finite bias and temperature [15].

In Fig. 11, we show the bias dependence of the current deviation from the TKE regime, $I - \frac{2}{M}G_0V_b$, for $M = 3, 4$. The data show a clear power-law behavior, particularly for bias values V_b that are not excessively small (such that the signal-to-noise ratio is reliable). In the displayed cases, the deviation of the current from the power-law fits is below the numerical precision $\sim 10^{-3}$.

In all cases, we observe a non-Fermi liquid scaling which significantly deviates from the cubic FL behavior of the current V_b^3 . However, the fitted exponents do not match the RG predicted values $\alpha + 1 = 3 - 4/M$. The absence of a clear separation of energy scales in the problem might be a source of deviation from the perturbative RG analysis. Moreover, close to the charge degeneracy point, intermediate fixed points are believed to emerge [11]. Finally, the fitted exponents seem to depend continuously on the coupling strength Γ and, while this analysis has shed light on a non-Fermi liquid behavior, further analysis is needed to understand these power-law corrections.

D. Breakdown of the TKE caused by a Majorana energy splitting

Here we investigate the effect on low-bias transport of an energy splitting between the subgap states of the lower and upper nanowires. In our modeling, this splitting is achieved by increasing the chemical potential μ_{sys} of the Kitaev chain of the lower wire, coupling the MZMs together and raising the energy of the corresponding fermionic level to $\epsilon_{0,\downarrow} = 0.08t_0$. The energy of the subgap state of the upper wire is $\epsilon_{0,\uparrow} \sim 10^{-5}t_0$, as in all other numerical results. We consider $M = 3$ leads and two different coupling configurations: in configuration A, both MZMs in the upper wire are coupled to the corresponding leads ($\alpha = 1, 2$), while the trivial subgap state in the lower wire is coupled to a single

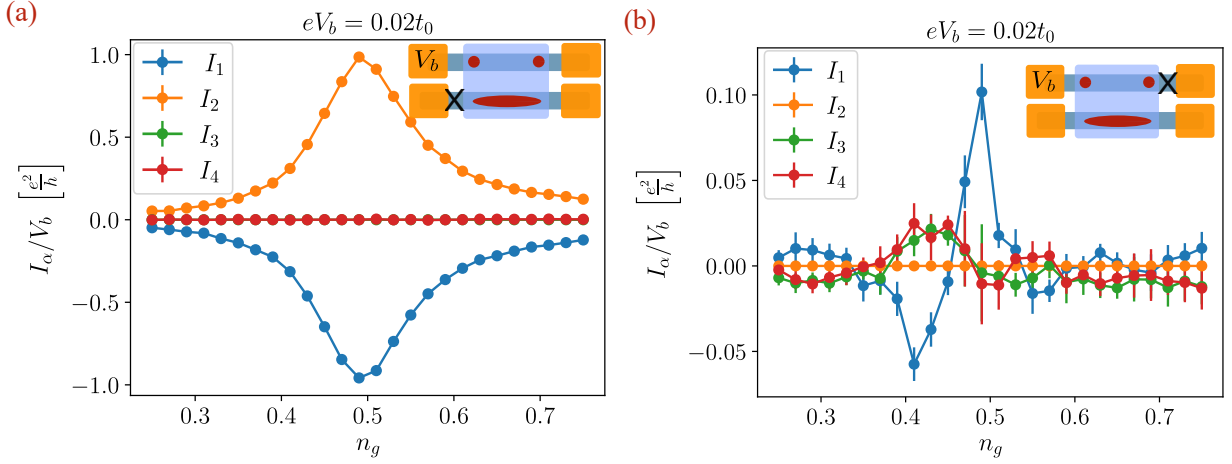


Figure 12. Current as a function of the induced charge n_g around the charge degeneracy point. A small voltage bias $eV_b = 0.02t_0$ is set on lead 1. In the upper nanowire the lowest energy state is a superposition of two MZM while in the lower one there is a subgap state of energy $\epsilon_{0,\downarrow} = 0.08t_0$. The coupling with the connected leads is $\Gamma = 0.04t_0$ (a) configuration A, with lead 3 decoupled. (b) configuration B, with lead 2 decoupled. Notice the different amplitude of the current in the two panels.

grounded lead; in configuration B, only the biased lead ($\alpha = 1$) is coupled with the upper wire, while the lower one has both leads 3 and 4 attached.

The results for configuration A are shown in Fig. 12(a), where we plot the current on all four leads as a function of the induced charge n_g . The voltage bias $eV_b = 0.02t_0$ is smaller than the energy $\epsilon_{0,\downarrow}$ of the subgap state in the lower wire. Consequently, there is almost no current flow in lead 4 (the only coupled to the lower wire) and the system behaves effectively as a two terminal device. Indeed, $I_{1/2}/V_b \simeq e^2/h$ at the charge degeneracy point, as we expect from resonant tunneling through a single pair of MZMs [64]. The asymmetry of the peak around $n_g = 0.5$ is due to faster cotunneling processes in the odd-parity Coulomb diamond (see Ref. [17]). I_1 and I_2 are almost identical but for the sign, since I_1 is an ingoing current, while I_2 is outgoing.

Figure 12(b) shows our results for configuration B. First, observe that the amplitude of the current signal is suppressed by a factor of 10 with respect to configuration A, missing a resonant state that can mediate transport. Moreover, the current sign changes multiple times as we tune n_g , with some similarities to Ref. [24], as different processes become dominant when the energies of the SC island many-body states cross the Fermi level of the leads. Furthermore, the equilibration time also increases, with respect to configuration A, maybe due to slow charge fluctuations between the leads and the superconductor. In both cases, the current signal we observe is markedly different from the corresponding behavior for the TKE, Fig. [5] of the main text, as the degeneracy at the heart of TKE is broken. In an experimental setup, an accidental degeneracy between trivial subgap states would be easy to remove by tuning external gates, while a robust observation of the features presented in the main text would be a strong smoking gun for the presence of MZMs in the system.

Finally, we investigate transport in a configuration where the upper and lower nanowires are degenerate but with a finite overlap between the MZMs, thus creating finite-energy subgap states in both wires. In particular, we consider $\epsilon_{0,\sigma} = 0.08t_0$ for both wires and $M = 3$ leads, where $\Gamma_2 = 0$ and $\Gamma_{\alpha \neq 2} = 0.04t_0$. Figure 13 reports the current on each lead as a function of n_g . With respect to the corresponding data in Fig.[5] of the main text, there is a clear shift of the charge degeneracy point to $n_g \sim 0.6$ due to the finite energy of the state mediating transport. However, the most striking difference is the strong suppression of the current far from the charge resonance. On the contrary, when the current is mediated by MZM and the TKE is expected to take place, a sizable nonzero current flows also deep in the Coulomb valley, even when transport is probed at energies above the T_K .

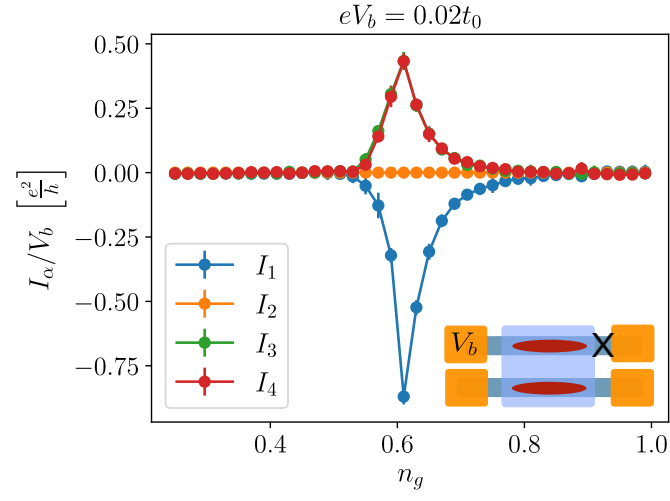


Figure 13. Local and nonlocal linear conductance I_α/μ_1 as a function of n_g , for a configuration with $M = 3$ leads and subgap states with a finite energy $\epsilon_{0,\sigma} = 0.08t_0$.